International Information and Engineering Technology Association
Advancing the World of Information and Engineering

Traitement du Signal
Vol. 41, No. 6, December, 2024, pp. 3313-3326
Journal homepage: http://iieta.org/journals/ts

A Novel Image Processing-Based Method for Wind-Induced Vibration Response Prediction and Structural Monitoring of Long-Span Bridges

Yingying Wang*, Youlai Qu, Yongbao Jiao

China Electric Construction Road and Bridge Group Corporation, Urumqi 830000, China

Corresponding Author Email: bearxt@163.com

https://doi.org/10.18280/ts.410647

Received: 10 May 2024
Revised: 8 October 2024
Accepted: 27 October 2024
Available online: 31 December 2024

Keywords:
long-span bridges, wind-induced vibration, structural monitoring, image processing, WOA

ABSTRACT

As a crucial component of modern transportation infrastructure, long-span bridges are subject to wind-induced vibrations that pose a key issue in structural safety studies. Wind-induced vibrations not only lead to dynamic deformation of the bridge but may also cause structural fatigue and failure. Therefore, accurately predicting and monitoring the wind-induced vibration responses is essential for ensuring the safe operation of bridges. With the rapid development of Digital Image Correlation (DIC) technology and machine learning algorithms, the integration of image processing and intelligent algorithms for monitoring and predicting wind-induced vibrations of long-span bridges has emerged as a promising research direction. Although significant progress has been made in monitoring and analyzing wind-induced vibrations, traditional methods often struggle with accurately capturing the evolution of minute deformations and achieving efficient predictions, thus limiting their practical application. This paper proposes a novel method for wind-induced vibration response prediction and structural monitoring of long-span bridges based on image processing. First, DIC technology is used to characterize the structural evolution of the bridge during wind-induced vibrations, capturing small deformations and local deformation features. Then, an image processing algorithm is applied to measure and calculate the structural evolution during the vibration response, enabling a quantitative analysis of the damage caused by wind load. Finally, by combining Whale Optimization Algorithm (WOA), Temporal Convolutional Network (TCN), and Self-Attention (SA) mechanism, a prediction model is developed to accurately forecast the bridge's dynamic response behavior under varying wind speeds. The study shows that this method effectively captures the spatiotemporal evolution characteristics of the wind-induced vibration process, enhancing the accuracy and reliability of the predictions, thus providing a scientific basis for the health monitoring and maintenance of long-span bridges.

1. INTRODUCTION

High-pier large-span rigid frame bridges, due to their characteristics of large span and high piers, have unique advantages when crossing rivers, valleys, and other complex terrains. Most of the western regions of China are mountainous and feature many valleys, where the canyon wind effect is significant. This special topography causes the airflow to be constrained as it passes through the canyon, resulting in a significant increase in wind speed and the formation of localized strong winds. For bridges that are not yet fully formed, due to insufficient stiffness and poor stability, their sensitivity to wind loads during construction is extremely high. In particular, phenomena such as buffeting and flutter can severely impact construction safety and may even cause structural disasters under extreme conditions. In this case, predicting the wind-induced vibration response of the bridge becomes a key technological means to ensure construction safety and the smooth progress of the project.

With the increasing importance of large-span bridges in modern transportation, their vibration response under wind loads has become a research hotspot in the field of structural engineering [1-4]. Wind-induced vibration is a common dynamic effect of long-span bridges in high-wind environments. In severe cases, it may lead to structural fatigue or even catastrophic accidents [5, 6]. Therefore, real-time monitoring and accurate prediction of the wind-induced vibration response of large-span bridges, especially the structural evolution behavior under wind loads, is crucial for ensuring the safety and durability of the bridge [7, 8]. However, due to the complexity of large-span bridge structures and the variability of wind-induced effects, how to accurately assess and predict their wind vibration response remains a challenge that needs to be addressed.

Although many studies on bridge wind-induced vibration response analysis and health monitoring have been conducted in recent years, existing prediction and monitoring methods still have certain limitations [9-11]. On one hand, traditional structural health monitoring methods often rely on sensors and physical models, which are often unable to effectively capture the early evolution of small deformations and the details of local deformations, leading to significant errors in the prediction of wind vibration responses [12-16]. On the other hand, image processing-based monitoring methods can capture more detailed deformation information, but how to combine this image data with time-series data to improve the accuracy and efficiency of prediction models remains a technical challenge [17-22]. In addition, existing wind vibration response prediction models often overlook the structural evolution characteristics under wind load, making it difficult to accurately reflect long-term dynamic changes.

The main research content of this paper includes three aspects: First, the structural evolution detection of the wind-induced vibration response of large-span bridges based on DIC technology, extracting the small deformations and local deformation information during the wind vibration response process; Second, using image processing algorithms to precisely measure and calculate the structural evolution of the wind-induced vibration response of large-span bridges, obtaining the dynamic strain and displacement distribution under wind load; Finally, combining WOA with the TCN-SA model to predict the wind-induced vibration response, efficiently capturing the temporal evolution patterns of the bridge structure under wind load. This study not only provides a novel computational framework for predicting the wind vibration response of large-span bridges but also offers more accurate theoretical and technical support for bridge structural health monitoring and wind vibration protection, with significant academic value and practical application prospects.

2. STRUCTURAL EVOLUTION AND WIND-INDUCED VIBRATION DETECTION IN LARGE-SPAN BRIDGES USING DIC

Due to their complex structure, large spans, and significant wind load effects, the wind-induced vibration response of large-span bridges often presents nonlinearity and time-varying characteristics. Traditional monitoring methods may not be able to comprehensively capture the dynamic behavior of bridges under different wind conditions. Therefore, this paper first performs structural evolution characterization and detection of the bridge's wind-induced vibration response, which helps reveal the long-term changes in the bridge structure under wind loads, local damage, and other possible structural changes, thus providing more reliable initial data and model input for subsequent wind vibration response prediction.

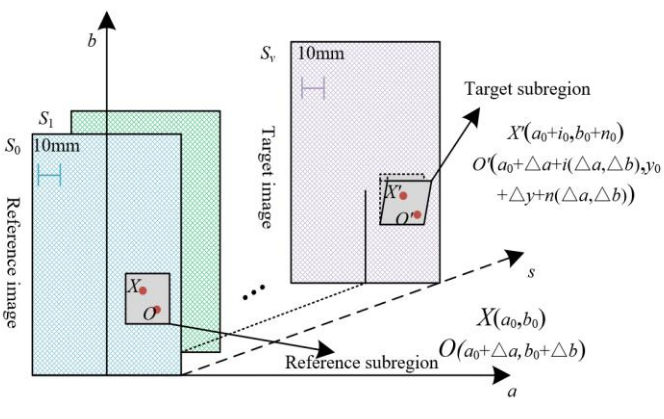

Figure 1. Schematic of large-span bridge before and after wind response

In order to obtain the global and local displacement of the bridge surface under wind vibration, this paper uses DIC technology to measure the concrete surface of the large-span bridge. Specifically, random speckle patterns are applied to the bridge surface, and images are captured at different time points. By comparing the gray scale changes between the pre- and post-deformation speckle images, the displacement field of the structure is calculated. This method allows for accurate acquisition of the global deformation information of the bridge under wind load, including displacement vectors and deformation conditions in each local area. By comparing deformation data at different time points, the time-varying characteristics of the bridge's wind vibration response are further revealed, especially capturing dynamic deformations and local vibration modes induced by wind loads. Figure 1 shows a schematic diagram of the wind-induced vibration response of the large-span bridge specimen before and after deformation. Let the center points of the reference subregion and target subregion be points X and X', respectively. The displacement of the reference subregion is the coordinate difference between points X and X', denoted as (i_0, n_0). The coordinate differences from the center point X within the subregion are denoted as $(\triangle a, \triangle b)$. The displacement of any point O is represented by $i(\triangle a, \triangle b)$, $n(\triangle a, \triangle b)$, which corresponds to the structural deformation information of the subregion. The gray scale value of each pixel in the reference subregion is denoted as $d(a_u, b_k)$, and the gray scale value of each pixel in the target subregion is denoted as $h(a_u^{'}, b_k^{'})$. The size of the subset is denoted as $(2L+1)\times(2L+1)$, and the coordinates (a_u, b_k) and $(a_u^{'}, b_k^{'})$ of the subset are directly related to the deformation occurring between images. The average gray scale values of the reference and target subregions are denoted as dl and hl, respectively. The introduced DIC image algorithm can be represented by the sequence correlation operation function Z_{CVZZ} as follows:

$$Z_{CVZZ}=\sum_{u=-L}^{L}\sum_{k=-L}^{L}\left\{\frac{\left[d\left(a_u,b_k\right)-d_l\right]\times\left[h\left(a_u^{'},b_k^{'}\right)-h_l\right]}{\Delta d\times\Delta h}\right\}=$$
$$\sum_{u=-L}^{L}\sum_{k=-L}^{L}\left\{\frac{d\left(a_u,b_k\right)-\frac{1}{\left(2L+1\right)^2}\sum_{u=-L}^{L}\sum_{k=-L}^{L}d\left(a_u,b_k\right)}{\sqrt{\sum_{u=-L}^{L}\sum_{k=-L}^{L}\left[d\left(a_u,b_k\right)-d_l\right]^2}}\times\right. \tag{1}$$
$$\left.\frac{h\left(a_u^{'},b_k^{'}\right)-\frac{1}{\left(2L+1\right)^2}\sum_{u=-L}^{L}\sum_{k=-L}^{L}h\left(a_u^{'},b_k^{'}\right)}{\sqrt{\sum_{u=-L}^{L}\sum_{k=-L}^{L}\left[h\left(a_u^{'},b_k^{'}\right)-h_l\right]^2}}\right\}$$

3. STRUCTURAL ANALYSIS AND WIND RESPONSE MEASUREMENT OF LARGE-SPAN BRIDGES VIA IMAGE PROCESSING

The image processing-based structural evolution measurement and calculation of wind vibration response further improve the accuracy and measurement efficiency of the bridge's wind vibration response. This paper achieves precise capture and real-time monitoring of the small deformations on the bridge surface using high-precision camera equipment and image analysis algorithms. Compared to traditional sensor technologies, this method offers higher flexibility and adaptability, enabling the acquisition of more comprehensive and detailed wind vibration response data without contacting the bridge structure. Especially for large-span bridges, image processing can effectively avoid measurement errors caused by sensor installation limitations or environmental interference, thus providing more valuable data support for accurate wind vibration response prediction.

To extract the evolution characteristics of the bridge structure under wind loads, this paper uses machine vision and image processing techniques to analyze the principal strain cloud map of the bridge under wind-induced vibration. First, the DIC technology is used to obtain the full-field principal strain field images of the bridge surface, which reflect the deformation and stress distribution of the bridge under wind loads. After obtaining the strain cloud map, machine vision technology in MATLAB software is applied to perform binarization processing by setting appropriate thresholds, separating high-strain areas corresponding to major deformations caused by wind vibration from low-strain areas corresponding to regions unaffected by wind vibration.

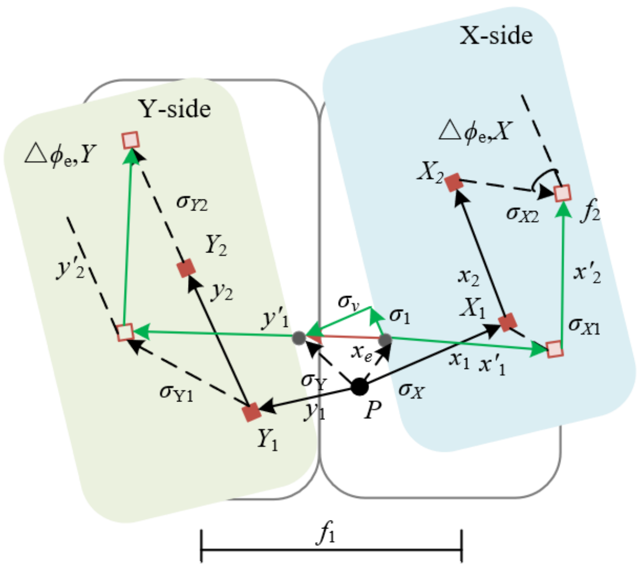

Figure 2. Calculation of displacement in wind-induced vibration of large-span bridges

Next, based on the displacement difference method, the calculation of normal and tangential displacements of the structural evolution of wind-induced vibration response in large-span bridges is performed. The schematic diagram of the calculation details is shown in Figure 2. After obtaining the full-field strain cloud map of the bridge surface, the image processing technique mentioned above is used to extract the structural deformation regions and stress concentration areas caused by wind vibration. Then, several key points along the path are selected as starting points for calculating the normal and tangential displacements of the structural evolution of the wind vibration response of large-span bridges. Around these reference points, adjacent points are selected to construct local geometric relationships and, combined with displacement information from the principal strain field, calculate the relative displacement of the structural evolution. Specifically, based on the displacement difference method, the horizontal and vertical displacements between different position points are compared, and the deformation distribution along the normal and tangential directions of the large-span bridge's wind-induced vibration response is calculated. When calculating the normal and tangential displacements, especially in the study of wind vibration response of large-span bridges, the displacement difference method can effectively handle local structural deformations and vibration modes caused by wind loads. The principal strain cloud map obtained by DIC technology can reflect the dynamic deformation information of the bridge surface due to wind vibration, while the displacement difference calculation method helps to further analyze the propagation trends of structural deformations by accurately capturing the relative displacements caused by the wind vibration response.

The principles for establishing the correlation evolution and displacement variables of the wind-induced vibration response structure of large-span bridges are based on the changes in the strain field, especially the local deformation evolution process caused by wind load-induced vibration. Traditional structural evolution variables usually rely on changes in macro structural deformations, such as a reduction in effective load-bearing area. However, DIC technology can finely capture the evolution of small deformations during the wind vibration response process, even identifying structural damage information at the micro-deformation stage. To effectively establish the correlation evolution and displacement variables for the wind vibration response of large-span bridges, this paper proposes using the coefficient of variation Z_n of the principal strain field as the damage variable. This is combined with the principal strain field of the wind vibration response obtained from DIC, and image processing and machine vision technologies are used to extract the evolution information of small deformations. The trend of changes in the coefficient of variation reflects the accumulation of structural damage under wind vibration. This allows for the gradual characterization of the deformation from small to significant during the wind vibration response process. Let the deformation area on the effective load-bearing area be represented by X_f, and the effective load-bearing area be represented by X. The initial deformation variable can be expressed as:

$$F = \frac{X_f}{X} \tag{2}$$

Assume the standard deviation and mean of the data are denoted by T and A^{-}, and the j-th maximum principal strain value in the maximum principal strain field of size $l\times v$ is denoted by A_j. By using Z_n as the damage variable, we have:

$$Z_n = \frac{T}{\bar{A}} \tag{3}$$

where,

$$T = \sqrt{\frac{1}{lv-1}\sum_{j=1}^{lv}\left(A_j - \bar{A}\right)^2} \tag{4}$$

$$\bar{A} = \frac{1}{lv}\sum_{j=1}^{lv} A_j \tag{5}$$

Through this position difference-based calculation method, combined with the evolution of principal strain, multidimensional evolution data for the wind vibration response of large-span bridges can be obtained.

4. WIND-INDUCED VIBRATION RESPONSE PREDICTION OF LARGE-SPAN BRIDGES BASED ON WOA-OPTIMIZED TCN-SA MODEL

This paper further proposes a wind-induced vibration response prediction method for large-span bridges based on the WOA-optimized TCN-SA model. The principal strain field data of the wind vibration response extracted by the aforementioned image processing technology (e.g., DIC), along with details such as the evolution of small deformations during the structural evolution process, will serve as input features for the model. These input data typically include the principal strain field at different time points during the wind vibration response, the coefficient of variation, and displacement variables related to the evolution of structural deformations. In the WOA-based TCN-SA model, these input features will be processed using the TCN and SA mechanism to capture the temporal and spatial correlations in the wind vibration response.

4.1 TCN

TCNs are a type of deep learning model designed for time-series data, particularly suitable for handling complex data with strong temporal dependencies, such as the wind vibration response of bridges. Unlike traditional recurrent neural networks (RNN) (e.g., Long Short-Term Memory (LSTM) and Gated Recurrent Unit (GRU)), TCN uses the architecture of Convolutional Neural Networks (CNN) to capture temporal features within sequences. TCN has advantages such as fewer parameters and faster training speeds, and it performs exceptionally well in handling long-term dependencies. The main components of TCN include causal convolution, dilated convolution, and residual connections.

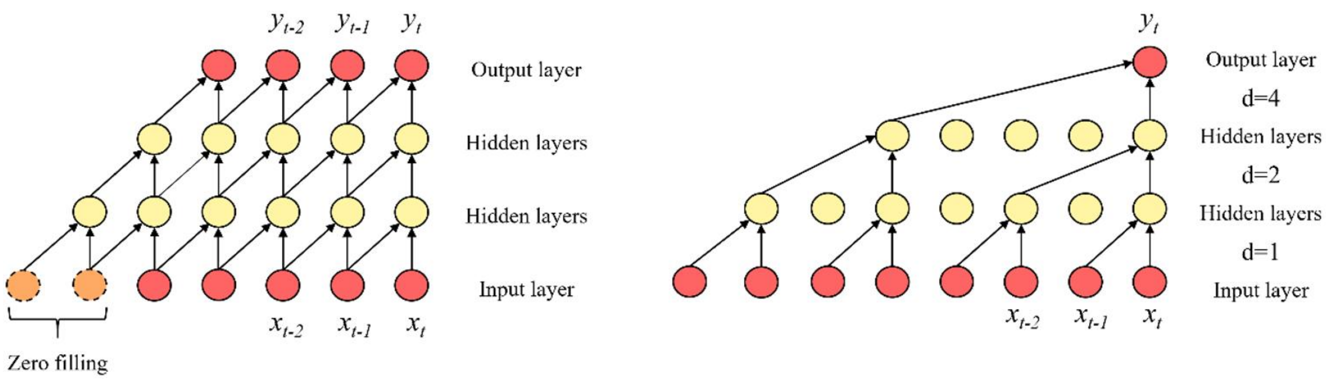

(a) Causal convolution (b) Dilated convolution

Figure 3. TCN model structure diagram

One of the key features of TCN is causal convolution, which ensures that the model's predictions are not influenced by future information. As shown in Figure 3 causal convolution only considers past and current information when performing convolution operations on each time point in the time series, avoiding future information leakage. This design allows TCN to effectively model the natural sequence of time series data when processing temporal data, preventing information leakage and ensuring the causality and reliability of the data predictions. Additionally, zero padding is applied at the front of the input sequence to ensure data completeness.

Let the input signal be $X=(x_1,x_2,x_3,\dots,x_{t-1},x_t)$, the output signal be $Y=(y_1,y_2,y_3,\dots,y_{t-1},y_t)$, and the convolution kernel be $K=(k_1,k_2,k_3,\dots,k_w)$, then the output y_t at time step t can be expressed as:

$$y(t)=\sum_{i=0}^{K-1} k(i)\cdot x(t-i) \tag{6}$$

where, K is the size of the convolution kernel, $k(i)$ is the i-th weight of the convolution kernel, and $x(t-i)$ is the input value at time step $t-i$.

Another core feature of TCN is dilated convolution, which introduces holes (also known as dilation rates) in the convolution kernel, enabling the model to handle longer sequences without significantly increasing computational complexity. The principle behind this is that by inserting zeros between elements of the convolution kernel, the input sequence undergoes spaced sampling, thus covering a wider input region during the convolution operation, effectively increasing the receptive field.

Typically, the dilation rate increases exponentially with the network layer depth and can be expressed as:

$$d_l=b^{(l-1)} \tag{7}$$

where, l is the network layer number, d_l represents the dilation rate of layer l, and b is the dilation factor.

The receptive field R_l of the l-th layer can be expressed as:

$$R_l=R_{l-1}+(K-1)d_l \tag{8}$$

The dilated convolution operation can be expressed as:

$$y(t)=\sum_{i=0}^{K-1} k(i)\cdot x(t-i\cdot d) \tag{9}$$

Residual connections are key structures for enhancing the performance and stability of TCN models. By introducing residual links, TCN can more effectively capture long-term dependencies in time series and avoid the vanishing gradient problem. Specifically, residual connections provide a direct path for the input signal to pass to subsequent layers, forming a residual learning path that alleviates the vanishing and exploding gradient issues that can occur in deep networks during training. This not only improves training efficiency but also enhances the generalization capability of the model, making TCN more effective for complex time series data tasks.

Let the input be x, and the output after the convolution layer be $F(x)$. Then the output of the residual block y can be expressed as (refer Figure 4):

$$y = \sigma(F(x) + x) \tag{10}$$

where, $\sigma(*)$ represents the activation function.

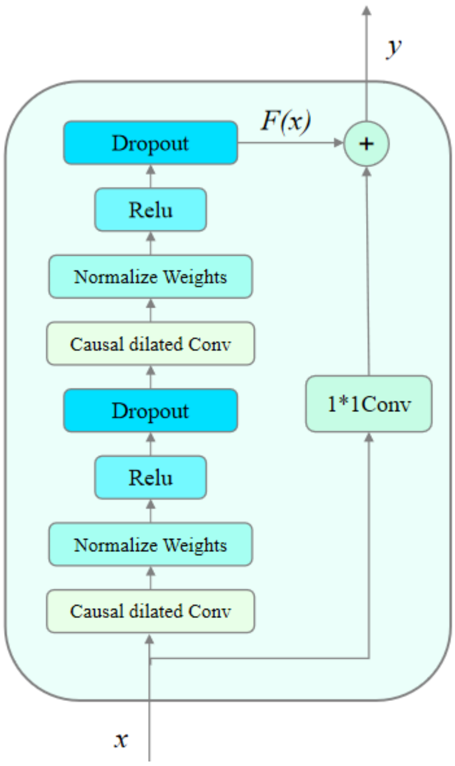

Figure 4. Residual block structure diagram

4.2 SA mechanism

The core idea of the SA mechanism is to establish global dependencies between elements in the input sequence, thus overcoming the limitations of local perception in traditional CNNs. Structural health monitoring data typically exhibit complex nonlinear patterns and long-distance dependencies. The SA mechanism, by evaluating the similarity or correlation between elements at different positions in the sequence, can adaptively adjust the importance weight of each element in the entire sequence. This mechanism effectively captures the intrinsic complex relationships in the data, helping to accurately understand and predict the changing trends of structural health states.

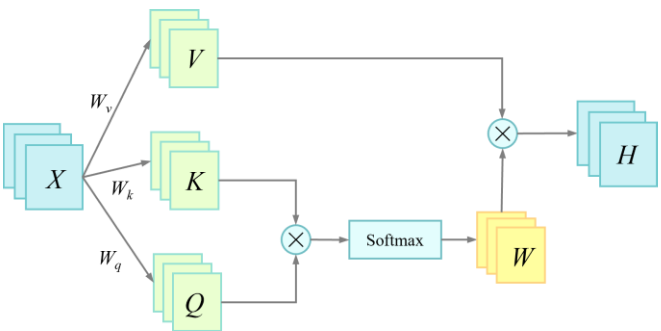

Figure 5. SA mechanism

The SA mechanism layer is shown in Figure 5. First, the input sequence X is linearly transformed into three new vector sequences: query Q, key K, and value V by applying three different weight matrices W_q, W_k, and W_v. The calculation formula is:

$$\begin{cases} Q = W_q X \\ K = W_k X \\ V = W_v X \end{cases} \tag{11}$$

Then, the similarity score between the Query matrix Q and the Key matrix K is computed using dot product. These scores are normalized by the softmax function to generate the SA weight matrix W, which indicates the importance of each position's information in generating the output. The normalization formula is:

$$W = Soft\max(\frac{QK^T}{\sqrt{d_K}}) \tag{12}$$

where, d_k is the dimension of K, used as a scaling factor.

Finally, by performing matrix multiplication between the SA weight matrix W and the value V, we obtain the output matrix H. This output matrix H integrates the information of all elements in the input sequence, but the representation of each element in H is the result of dynamically adjusting the weights based on its correlation with other elements in the sequence.

$$H = Attention(Q, K, V) = Soft\max(\frac{QK^T}{\sqrt{d_k}})V \tag{13}$$

The SA mechanism achieves effective capture of the correlations between internal elements of sequence data in this way, allowing the model to dynamically adjust the weights of different features, thereby more accurately understanding and processing the sequence data.

4.3 WOA

TCN models often have a large number of hyperparameters, such as learning rate, network depth, kernel size, number of kernels, and dilation factors. The quality of these parameters directly affects the performance and convergence speed of the model. Traditional grid search or random search methods perform poorly in high-dimensional and complex optimization tasks, while the WOA can search for the optimal solution by simulating the self-organizing and adaptive hunting behavior of whale groups. The optimization process is as follows:

Step 1: Encircle the prey

The main goal of this stage is to gradually approach and encircle the prey, i.e., search for potential optimal solutions within the search space. This process can be expressed by the following formula:

$$D' = \left| C \cdot \dot{X}^* - \dot{X}(t) \right| \tag{14}$$

$$\dot{X}(t+1) = \dot{X}^*(t) - A \cdot D' \tag{15}$$

where, D' is the distance between the whale individual and the prey, t is the iteration number, $\dot{X}(t)$ is the position vector of the whale at iteration t, and $\dot{X}^*(t)$ is the best position vector after t iterations. The coefficient vectors A and C are calculated as:

$$A = 2a \cdot r_1 - a \tag{16}$$

$$C = 2r_2 \tag{17}$$

where, a is a coefficient that decays from 2 to 0 as the iteration progresses, and r_1 and r_2 are random variables within [0,1].

Step 2: Bubble net attack

The whale surrounds the prey by releasing a spiral-shaped bubble net from the bottom up, thus roughly determining the location of the prey. Then, the whale group will continuously update their positions along the spiral bubble net to approach the target. This process can be expressed as:

$$\dot{X}(t+1) = \dot{D}' \cdot e^{bl} \cdot \cos(2\pi l) + \dot{X}^*(t) \tag{18}$$

$$\dot{D}' = \left| \dot{X}^*(t) \text{-} \dot{X}(t) \right| \tag{19}$$

where, $\dot{D}'$ is the current best distance between the whale and the prey, b is a constant defining the spiral turning, and l is a random number within [-1,1].

The whale continues to approach the prey by combining the strategies of shrinking the bubble net and spiraling upward along the bubble net. We simulate the probability of these two events both happening as 50%, expressed as:

$$\dot{X}(t+1) = \begin{cases} \dot{X}^*(t) \text{-} \dot{A} \cdot \dot{D} & p \prec 0.5 \\ \dot{D}' \cdot e^{bl} \cdot \cos(2\pi l) + \dot{X}^*(t) & p \geq 0.5 \end{cases} \tag{20}$$

where, p is a random number within [-1,1].

Step 3: Random search

To avoid getting stuck in local optima within the search space, the WOA introduces a random search mechanism, allowing the whale to jump out of the current area and explore a broader space. Specifically, when the coefficient vector $|A|$ is greater than 1, the whale will adopt the random search strategy. In this case, the whale's next position will not directly depend on the current optimal solution, but rather randomly select another whale as the guide to update its position. The random search process can be expressed as:

$$\dot{X}(t+1) = \dot{X}_{rand} - A \cdot \dot{D} \tag{21}$$

$$\dot{D} = \left| C \cdot \dot{X}_{rand} \text{-} \dot{X}(t) \right| \tag{22}$$

where, $\dot{X}_{rand}$ is the position vector of a randomly selected whale individual.

The overall process of WOA is shown in Figure 6.

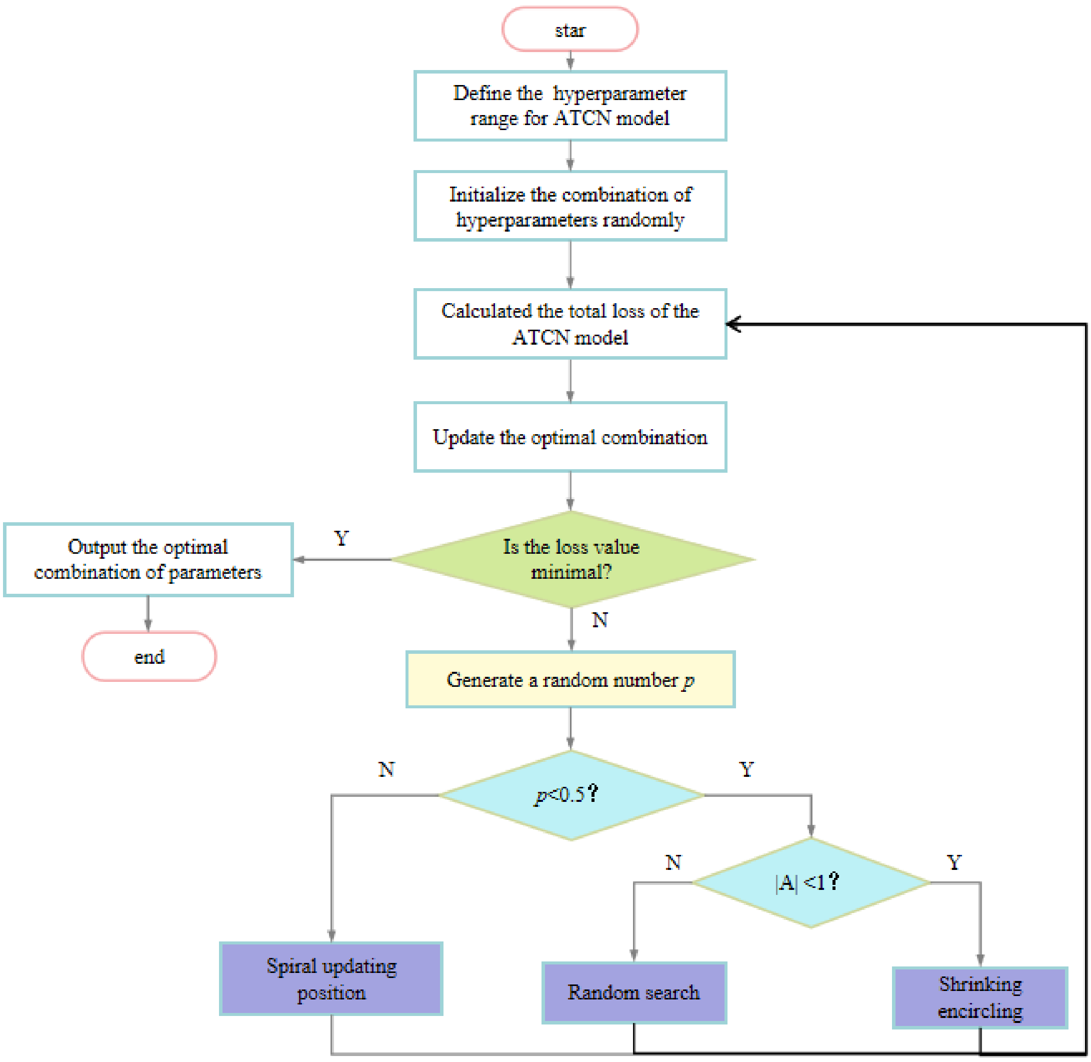

Figure 6. Flowchart of WOA

4.4 Model framework

The framework for the wind vibration response prediction algorithm of large-span bridges is shown in Figure 7. In this paper, we propose a WOA-optimized TCN-SA model to predict the vibration response of bridges under wind load. This model combines the advantages of TCN and SA, while using the WOA to finely tune the model parameters to achieve optimal prediction performance. In terms of data collection, we placed 2D and 3D anemometers on both sides of the bridge to fully capture the wind field information, and four accelerometers were installed to monitor the vibration acceleration of the bridge in both the longitudinal and transverse directions. From the raw data sources, we selected the data subset closely related to the target task. These data provide rich inputs for the model, allowing it to learn the complex relationship between wind load and bridge vibration. During the model training phase, we first pre-train the model using the collected wind speed data and bridge vibration acceleration data to preliminarily establish the mapping relationship between wind load and bridge vibration. Subsequently, we start the WOA process. This process simulates the whale hunting behavior through strategies such as encircling, spiral updating, and random searching, and automatically searches for the optimal model parameter combinations in the parameter space. This optimization process not only reduces the manual tuning workload but also significantly improves the efficiency of parameter configuration, enabling the model to better adapt to the complex and variable wind field environment and bridge vibration characteristics. Through training and optimization, the TCN-SA model can accurately predict the vibration response of bridges under different wind conditions, providing strong support for the safety assessment and maintenance management of bridges.

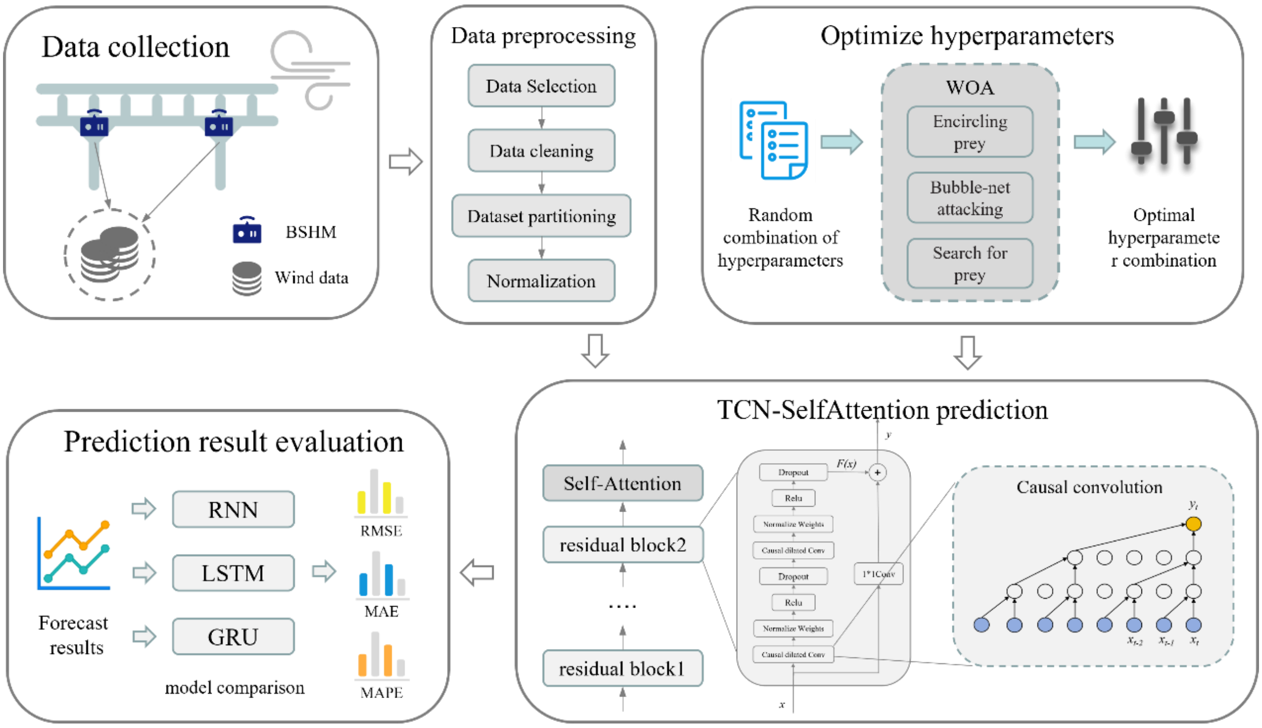

Figure 7. Large-span bridge wind vibration response prediction algorithm model framework

5. EXPERIMENT AND DISCUSSION

5.1 Experiment setup

The experimental dataset used in this paper is the bridge wind vibration response dataset after preprocessing, with an 8:2 ratio for training and testing. Additionally, three commonly used time series forecasting models are selected as comparison algorithms, namely RNN, LSTM, and GRU.

5.2 Hyperparameter optimization

In this study, the WOA is used to optimize the key hyperparameters of the model, including the number of convolutional kernels, kernel size, and dilation factor size. These hyperparameters significantly affect the model's performance, determining its complexity, receptive field size, and the level of detail in feature extraction. By using WOA for hyperparameter optimization, the best hyperparameter combination is automatically selected to achieve optimal performance for a specific prediction task. The optimization process is as follows:

(1) Initialization: Set the population size to 20 and randomly generate a population, where each individual represents a different hyperparameter combination. Each individual contains three hyperparameters: the number of convolutional kernels, kernel size, and dilation factor size. All initial values are randomly selected within reasonable ranges.

(2) Fitness Calculation: For each individual (i.e., hyperparameter combination), we construct the corresponding TCN model and train it. The model's prediction error on the validation set is calculated as the fitness value, measuring the performance of the hyperparameter combination for the current task.

(3) Whale Optimization: Based on the fitness calculation, WOA simulates the bubble net strategy used by humpback

whales during hunting to update the position of each individual. This process includes whale encircling prey, bubble net attack, and exploration behaviors, progressively iterating to update the hyperparameter combination. In each iteration, individuals update their positions according to the fitness values, choosing the better direction for parameter adjustment until termination conditions are met.

The specific hyperparameter optimization range and results are shown in Table 1.

Table 1. Hyperparameter optimization results

Parameter Name	Optimization Range	Optimized Result
Number of kernels	[8,128]	48
Kernel size	[1,5]	4
Dilation factor	[1,4]	2

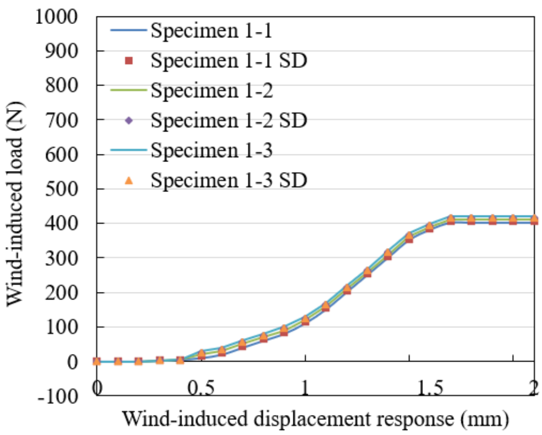

(a) Specimen 1

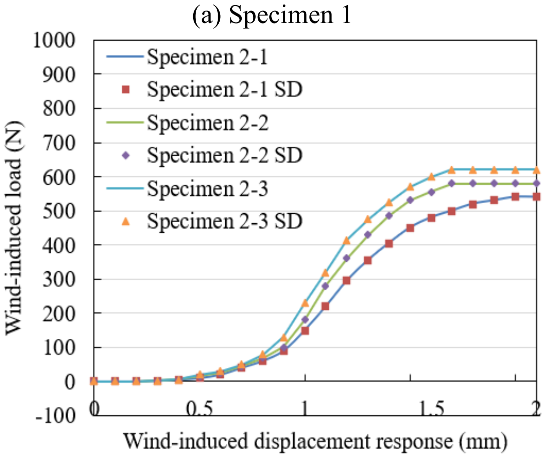

(b) Specimen 2

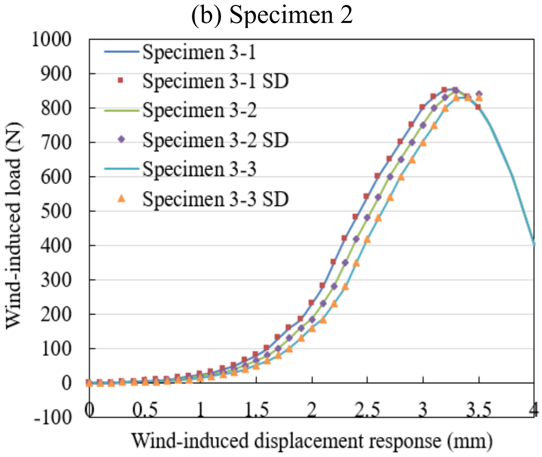

(c) Specimen 3

Figure 8. Wind load - wind vibration response displacement curves for three specimens

5.3 Experimental results

This paper uses the WOA-optimized TCN-SA model, combined with DIC technology and image processing algorithms, to analyze the wind load and wind vibration response displacement data of three specimens. By analyzing the data shown in Figure 8, we can gain an in-depth understanding of the dynamic response behavior of bridge structures under wind load and their temporal evolution patterns.

For Specimen 1, the data shows a trend where the wind vibration response displacement gradually increases with the increase in wind load. Specifically, the wind vibration response displacements of Samples 1-1, 1-2, and 1-3 show a clear nonlinear growth. Taking Sample 1-1 as an example, as the wind load increases from 0 to the maximum value, the displacement increases from 0 to 400mm. The standard deviation (SD) also increases with the wind load, particularly at higher wind loads, where the SD increases significantly (e.g., when the wind load is 2, SD is 5, and at the maximum, SD reaches 405). This indicates that under high load, the fluctuations and uncertainties in the wind vibration response also increase.

Specimen 2's data also shows a gradual increase in the wind vibration response displacement as the wind load increases. For Sample 2-1, the displacement starts from 0 and gradually increases with the wind load, especially when the wind load reaches 2, where the displacement reaches a large value, with a maximum displacement of 540mm. The standard deviation increases with the wind load, reflecting the increased fluctuations in structural response under high wind loads. This suggests that an increase in wind load not only enlarges the bridge's vibration displacement but also amplifies the fluctuation in the structural response, highlighting the need to pay special attention to these response characteristics under high loads during design and monitoring.

Specimen 3's wind vibration response data is more complex, with obvious periodic oscillations. Particularly, the wind vibration response data for Samples 3-1, 3-2, and 3-3 exhibit strong oscillatory characteristics, especially under high wind loads, where the displacement response shows a relatively stable growth trend. For Sample 3-1, the wind vibration response displacement increases from 0 to a maximum of 850mm. As the wind load increases, the response displacement gradually reaches a saturation point, and when the wind load is 2, the displacement reaches the maximum and stabilizes in subsequent load increases. This suggests that Specimen 3's response might stabilize after experiencing certain wind loads and is no longer increasing significantly.

From the data in Figure 9, it can be observed that there are certain differences in the wind vibration response displacement values measured by physical measurements, deep learning methods, and the method used in this paper under different load conditions for Specimens 1-1, 1-2, and 1-3. For Specimen 1-1, as the wind vibration load increases from 0 to 1, the physical measurement data show a relatively steady downward trend, with the wind vibration response displacement decreasing from 1500 mm to 400 mm. The measurements from the deep learning method and the method in this paper are slightly lower, especially when the wind load is 0.5, where the displacement measured by deep learning and the method in this paper are 1300 mm and 1200 mm, respectively, clearly lower than the physical measurement of 1500 mm. A similar trend is observed for Specimens 1-2 and

1-3, where the physical measurement method consistently gives higher displacement values, while the measurements from the deep learning method and the method in this paper exhibit some deviation, typically being slightly lower than the physical measurements under the same load. For example, the physical measurement value for Specimen 1-3 at a wind load of 1 is 2100 mm, while the values from deep learning and the method in this paper are 2050 mm and 2000 mm, respectively, indicating that the measurements from deep learning and this method are quite close under high wind loads.

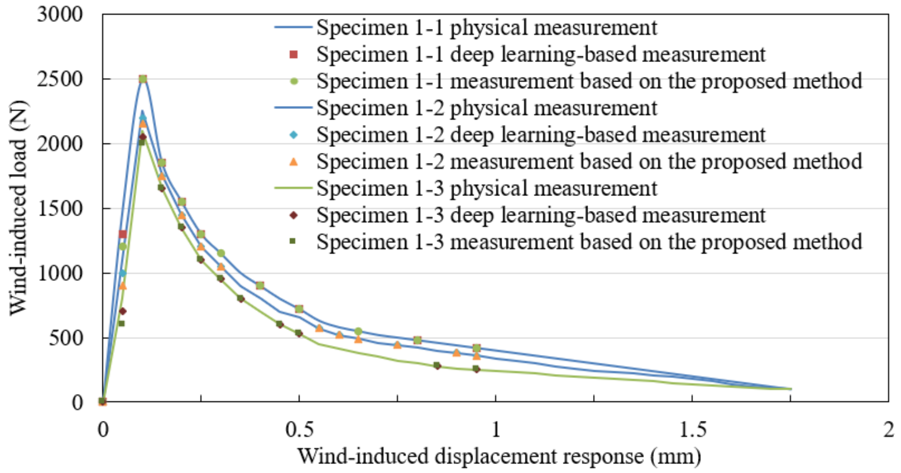

Figure 9. Wind vibration response displacement values based on DIC image results for different measurement methods

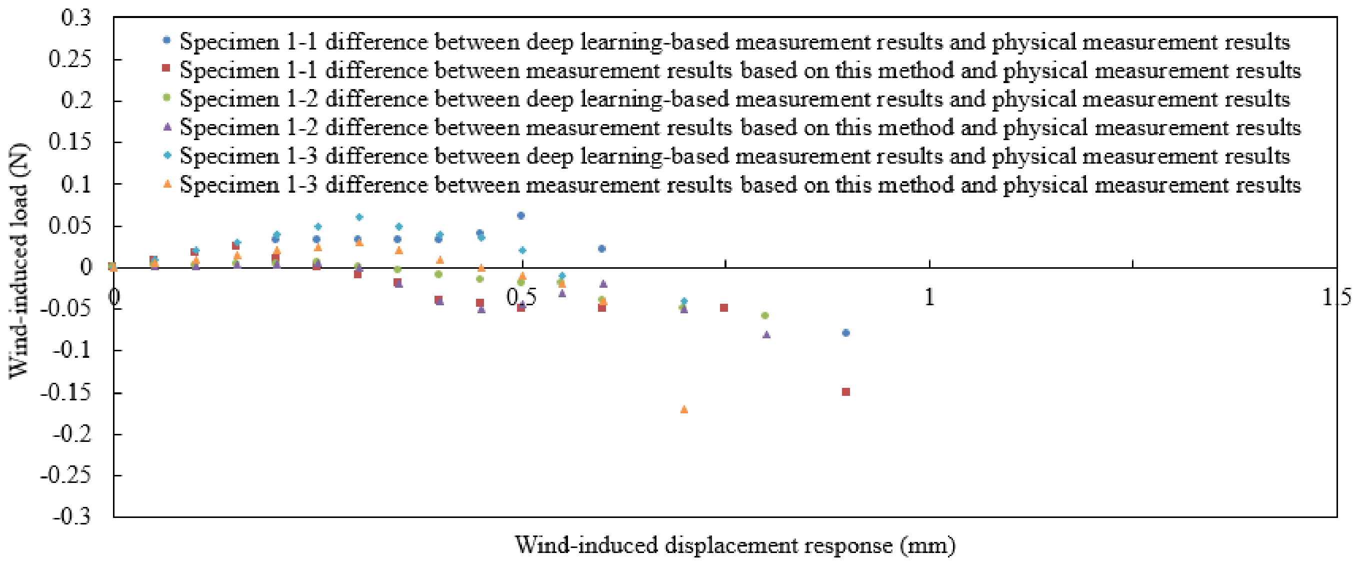

Figure 10. Comparison of calculation errors for different measurement methods

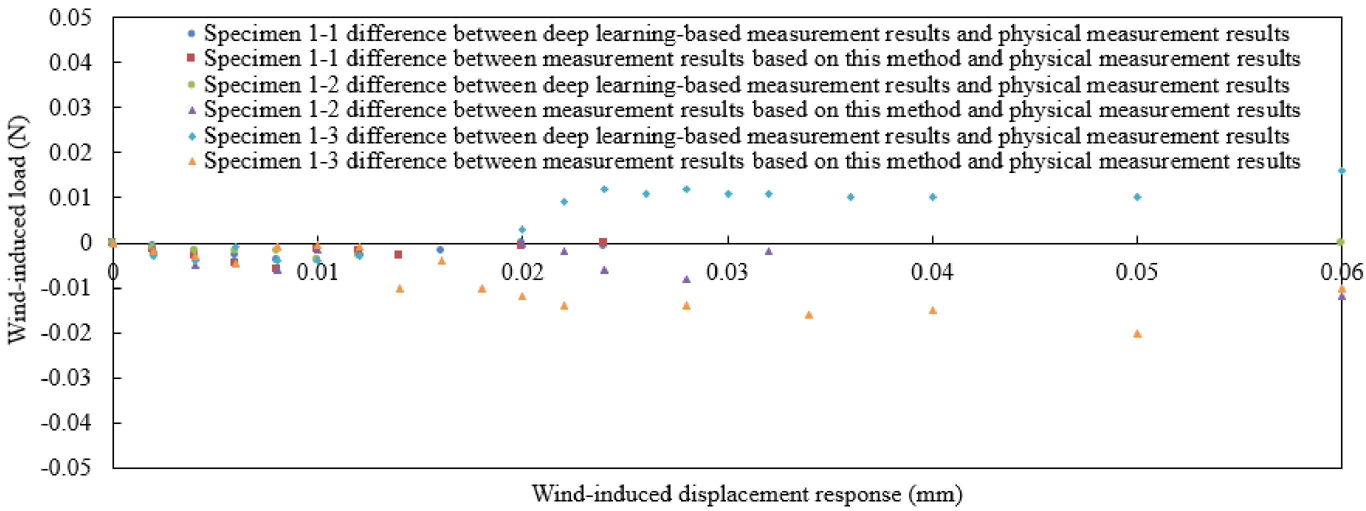

Figure 11. Comparison of calculation errors for different measurement methods with displacement less than 0.05 mm

According to the data in Figure 10, the error comparison results for Specimens 1-1, 1-2, and 1-3 under different measurement methods reveal the accuracy and consistency of different measurement methods. For Specimen 1-1, the difference between the measurement results from the deep learning method and the physical measurement increases gradually with the wind load. The difference ranges from 0 to 0.5 for the wind vibration response displacement, with the maximum difference being 0.06. This suggests that the error from the deep learning method is relatively larger under higher loads, especially under higher wind load conditions, where the error shows a significant increase. In contrast, the measurement error of the method in this paper is clearly smaller, with the difference fluctuating less between 0 and 0.5 for the wind load range, and the maximum difference is 0.05, demonstrating better measurement consistency and stability overall. For Specimen 1-2, the difference between the deep learning method and the method in this paper is relatively small, ranging from 0.001 to 0.02, indicating high accuracy under low wind loads. However, under higher loads, the difference for the method in this paper is slightly larger than that of the deep learning method, with the maximum difference being 0.045, but still within an acceptable range. For Specimen 1-3, the error for the deep learning method increases from 0.01 to 0.06, especially under high wind loads, where the error becomes more pronounced. In contrast, the error for the method in this paper remains smaller, with the maximum difference being only 0.01, and as the wind load increases, the error tends to stabilize, showing strong stability and high accuracy.

According to the data in Figure 11, for Specimens 1-1, 1-2, and 1-3, when the wind vibration response displacement is less than 0.05 mm, the differences between the measurement results from the deep learning method, the method in this paper, and the physical measurements show different error trends. First, for Specimen 1-1, the error for the deep learning method is small, fluctuating between 0 and -0.004, and the error is relatively stable between 0.01 mm to 0.03 mm of wind load. In comparison, the error for the method in this paper is slightly larger, fluctuating between -0.0015 and -0.006, but overall the variation is small, indicating that the measurement error for the method in this paper remains at a low level within this range. For Specimen 1-2, the error for the deep learning method is also small, with a difference range from -0.0012 to -0.004, indicating higher measurement accuracy under low wind loads. The difference for the method in this paper is larger, with a maximum of -0.008, but the variation remains within an acceptable range. Finally, for Specimen 1-3, the deep learning method's error is relatively stable in the 0.01 mm to 0.03 mm wind load range, fluctuating between -0.003 and 0.012. In contrast, the error for the method in this paper is more stable, fluctuating between -0.002 and -0.014, showing good consistency, especially where the error variation is relatively stable under most measurement conditions.

Further, we use the TCN-SA model proposed in this paper to predict the bridge's wind vibration response acceleration and compare the prediction results with those from three other algorithm models to determine the model's prediction performance. Also, to more accurately understand the bridge’s wind vibration response, we predict the different responses of four types of bridges under wind load: longitudinal acceleration, transverse acceleration, vertical acceleration, and torsional acceleration.

Figure 12 shows the scatter plot distribution of the predicted values versus the true values for the bridge's wind vibration response acceleration in different directions using the TCN-SA model. It can be observed that there is a linear correlation between the predicted and true values, and the distribution pattern of the predicted values aligns well with the true values, with low dispersion.

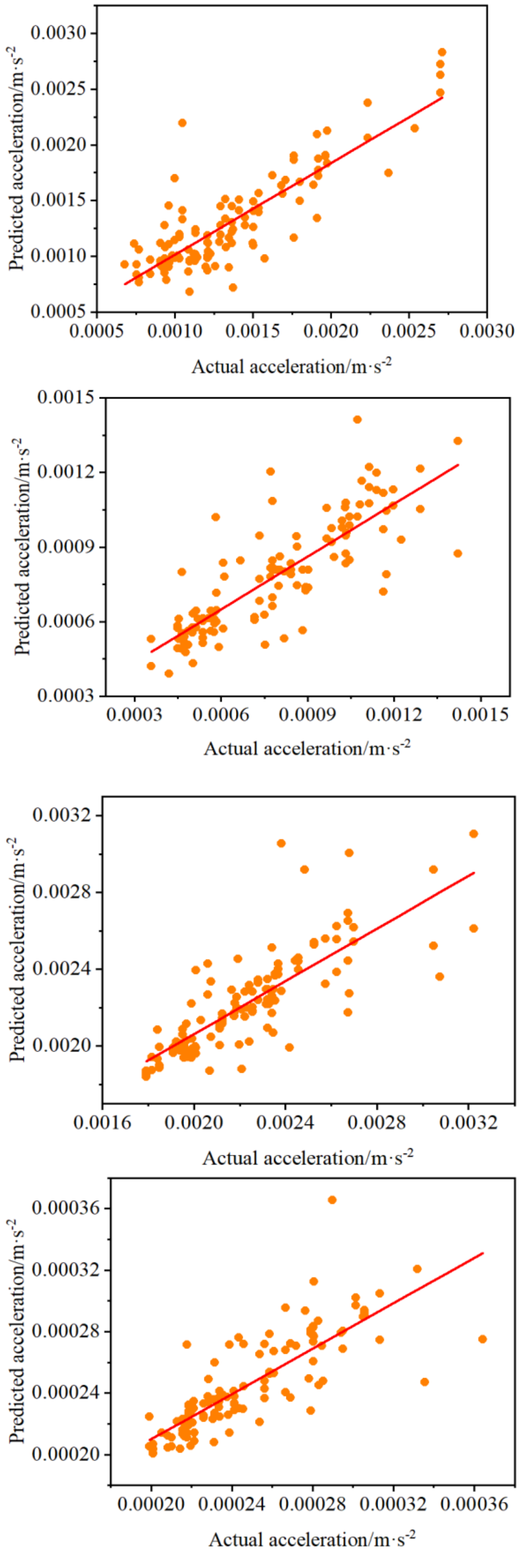

Figure 12. Scatter plot of true values and predicted values

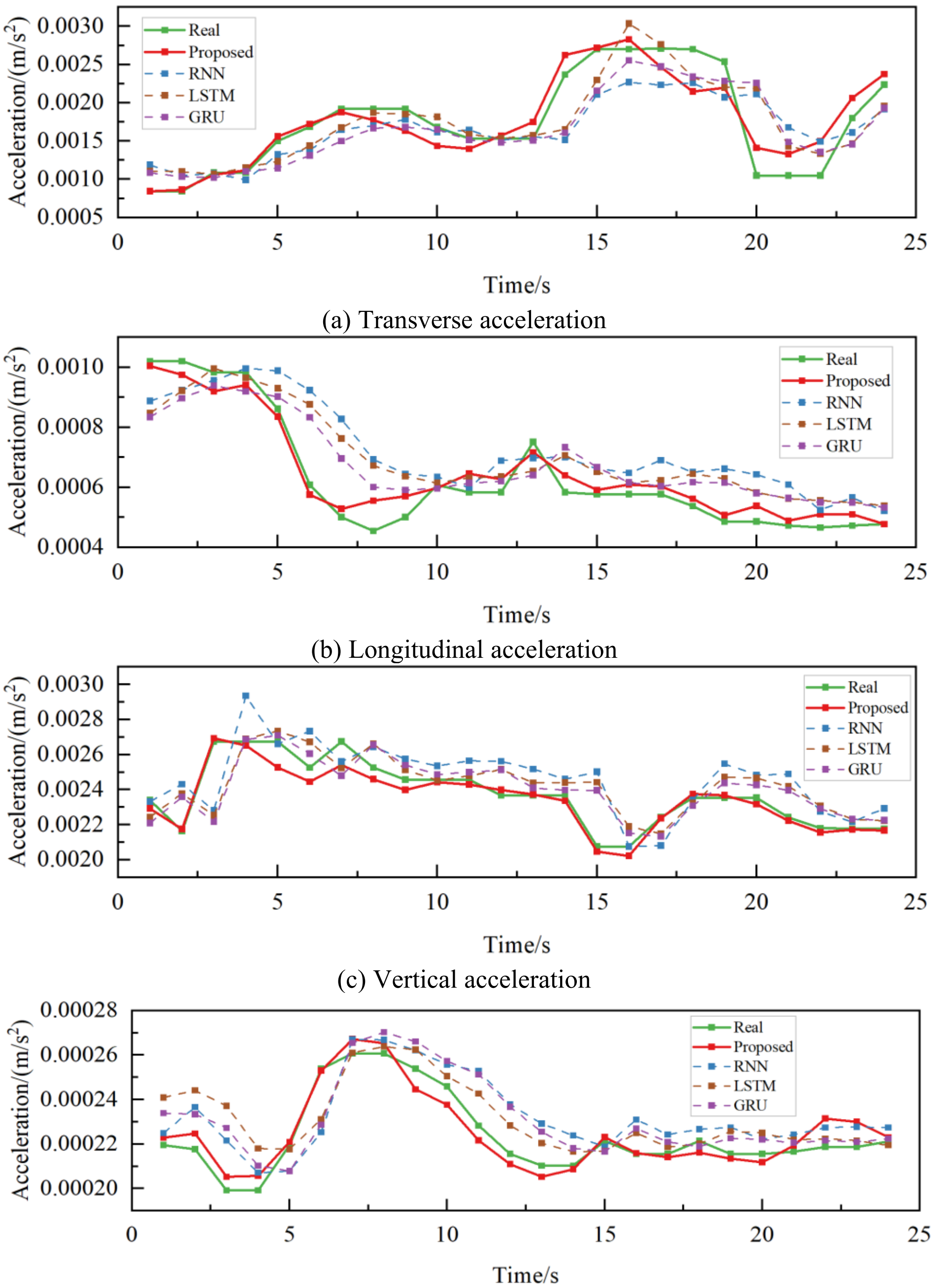

(a) Transverse acceleration
(b) Longitudinal acceleration
(c) Vertical acceleration
(d) Torsional acceleration

Figure 13. Comparison of prediction results for different models

Table 2. Evaluation metrics for different directions

Acceleration	Prediction Model	*MAE*/10^{-5}	*RMSE*/10^{-5}	*MAPE*/%
Transverse direction	*Proposed*	15.84	22.46	12.8
	RNN	22.47	28.86	18.9
	LSTM	21.48	27.23	18.2
	GRU	20.1	26.99	17.1
Longitudinal direction	*Proposed*	9.71	13.3	12.9
	RNN	13.3	17.04	19.1
	LSTM	11.58	15.36	16.4
	GRU	11.06	14.86	15.2
Vertical direction	*Proposed*	10.68	17.49	4.8
	RNN	14.65	21.11	6.4
	LSTM	13.58	19.55	5.9
	GRU	13.03	18.94	5.7
Torsional direction	*Proposed*	1.22	1.96	4.9
	RNN	1.61	2.25	6.3
	LSTM	1.42	2.11	5.6
	GRU	1.41	2.17	5.6

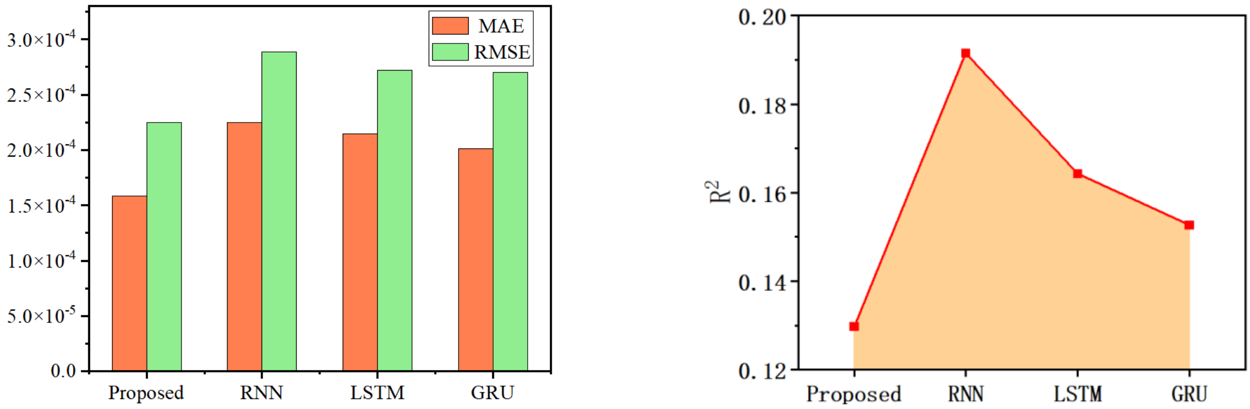

(a) Transverse direction

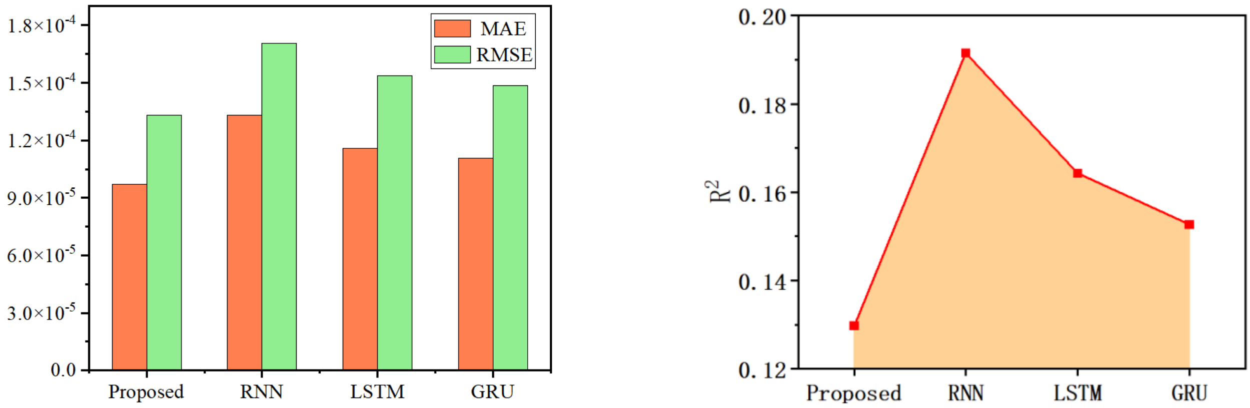

(b) Longitudinal direction

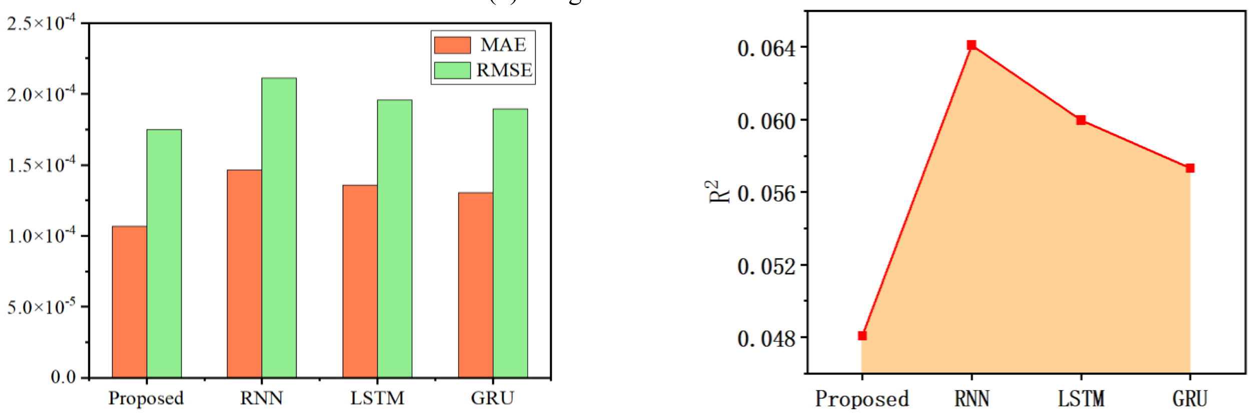

(c) Vertical direction

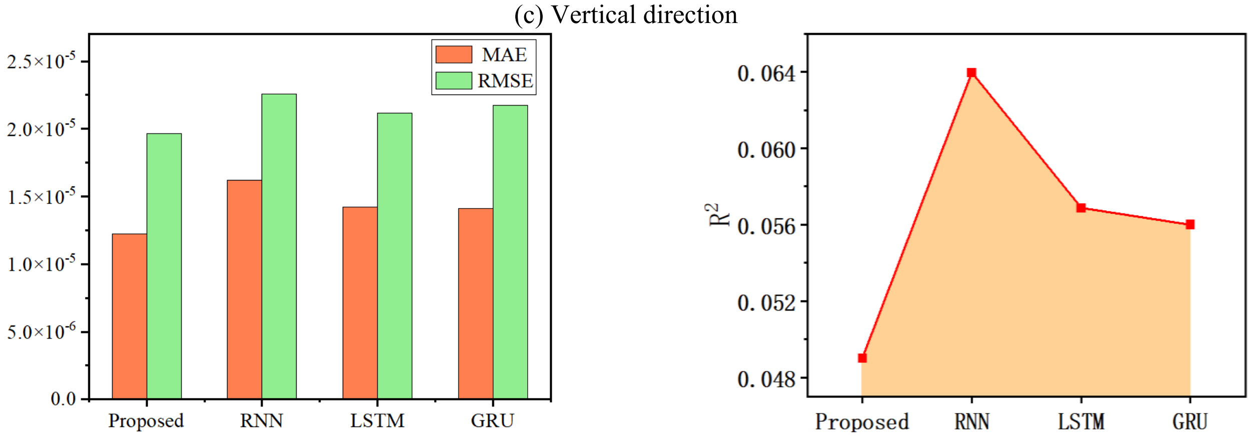

(d) Torsional direction

Figure 14. Evaluation metrics for different models

Figure 13 shows the comparison between the predicted and true values for bridge wind vibration response acceleration in four directions for each model. It can be observed that the TCN-SA model proposed in this paper consistently exhibits the best performance.

In this paper, we compare the performance of three other typical time series prediction algorithms, namely RNN, LSTM, and GRU. RNN is a neural network model specifically designed for sequence data, with a memory function that retains information from previous time steps and applies it in the current time step calculation. LSTM is a special type of RNN that introduces gating mechanisms (forget gate, input gate, and output gate) to capture and utilize long-term dependencies more effectively, thus alleviating the gradient vanishing and explosion problems that traditional RNNs face when processing long sequence data. GRU is also a type of recurrent neural network structure similar to LSTM but with a simpler design, containing only update and reset gates, resulting in fewer parameters and faster training speed. Figure 13 and Table 2 present the evaluation metrics for each model's prediction of bridge wind vibration response acceleration in four directions.

From Figure 14 and Table 2, it can be seen that for the evaluation metrics of bridge wind vibration response acceleration predictions in various directions, the TCN-SA model significantly outperforms the other three models, followed by the GRU and LSTM models, while the RNN model performs the worst. During training, the TCN-SA model uses a causal dilated convolution and residual connection structure. The causal dilated convolution introduces a dilation into the causal convolution, giving it a larger receptive field to capture long-term dependencies in the bridge wind vibration data. The residual connection adds the input from the previous layer directly to the current layer's output, avoiding the loss of information between network layers and alleviating the vanishing gradient problem. Moreover, the SA mechanism can automatically identify the important parts of the features and focus on significant features between different time steps, thereby capturing the potential relationships between the bridge's wind vibration response data more comprehensively and accurately. This results in the TCN-SA model achieving the best performance. The LSTM and GRU models show similar predictive performance. Compared to the traditional RNN model, both LSTM and GRU introduce gating mechanisms, which allow them to more effectively capture long-term dependencies in time series. The GRU model has a simpler structure than LSTM, removing the output gate and memory cell from LSTM, which reduces the parameter count and speeds up model training while still maintaining performance. The RNN model, due to its recurrent network structure, suffers from gradient vanishing or explosion problems, making it difficult to capture long-term dependencies in the data effectively, thus performing poorly in bridge wind vibration response prediction.

6. CONCLUSION

This study proposed a comprehensive monitoring and prediction method for the wind vibration response of large-span bridges under wind loads, combining DIC technology, image processing algorithms, and machine learning models. The research covers three main aspects: first, using DIC technology to characterize the structural evolution during the bridge's wind vibration response, accurately extracting small deformations and local deformation information; second, applying image processing algorithms to precisely measure the structural evolution during the wind vibration response, obtaining the dynamic strain and displacement distribution of the bridge under wind loads; and third, constructing a wind vibration response prediction model by combining WOA optimized TCN with SA, which efficiently captures the time-sequential evolution characteristics of the bridge structure under wind loads.

The study achieves significant progress in multiple areas. First, the DIC-based structural evolution characterization method effectively captures small deformations and local deformations of the bridge, filling the gap in traditional methods for early identification of small deformations and detection of local deformations. Second, the application of image processing algorithms enables more precise measurements of the dynamic strain and displacement distribution of the bridge's wind vibration response, providing rich data support for in-depth analysis of the structural impact of wind loads. Finally, the wind vibration response prediction method combining the WOA and TCN-SA model can accurately capture the time-sequential evolution characteristics under wind loads, significantly improving the accuracy and reliability of the wind vibration response prediction.

Overall, the proposed monitoring and prediction framework provides a more accurate theoretical basis and technical means for the health monitoring, structural evaluation, and maintenance of large-span bridges, offering high academic value and practical application prospects.

However, there are certain limitations in this study. First, although DIC technology and image processing algorithms can acquire fine strain fields and crack evolution information, challenges remain in processing image data at high speeds and applying these technologies in the complex environments of large-span bridges. Second, although the WOA-optimized TCN-SA model performs excellently in terms of prediction accuracy, the computational complexity during the model's training process is relatively high, which could create bottlenecks for the promotion of real-time monitoring and early warning systems. Therefore, future research could focus on improving the real-time performance and efficiency of image processing algorithms, optimizing the computational efficiency of machine learning models, and exploring the integration of more sensor and image data to form a more comprehensive and efficient monitoring and prediction system. Future research directions could include the following: (1) Strengthening multi-source data fusion techniques by combining traditional sensor data with image processing results to further improve the accuracy and real-time performance of wind vibration response monitoring and prediction. (2) Exploring more efficient algorithm optimization methods, particularly for large-scale structural prediction problems, to reduce computational complexity and improve model operability. (3) Conducting more experimental studies based on actual bridges to verify the application effects of the methods proposed in this paper in real-world environments, and proposing more personalized and targeted maintenance and reinforcement plans based on the bridge's specific operational conditions.

REFERENCES

[1] Qin, W.F., Tu, Z., Yu, S., Xie, J. (2023). Improvement of wind-induced responses of twin towers using modal substructure method with link bridges. Sustainability, 15(16): 12397. https://doi.org/10.3390/su151612397

[2] Huang, G., Liu, R., Liu, M., Zheng, H. (2021). Modeling and simulating nonstationary thunderstorm winds based on multivariate AR-GARCH. Journal of Wind

Engineering and Industrial Aerodynamics, 211: 104565. https://doi.org/10.1016/j.jweia.2021.104565

[3] Zhang, D., Li, N., Li, Z.X., Xie, L. (2020). Seismic performance of bridge with unbonded posttensioned self-centering segmented concrete-filled steel-tube columns: An underwater shaking table test. Soil Dynamics and Earthquake Engineering, 138: 106350. https://doi.org/10.1016/j.soildyn.2020.106350

[4] Xue, G., Miao, J., Zhang, D., Zuo, S., Zhang, C., Li, N. (2025). Seismic acceleration response prediction method of the PSCFST bridge based on TCN. Journal of Constructional Steel Research, 224: 109147. https://doi.org/10.1016/j.jcsr.2024.109147

[5] Zhang, D., Chen, Y., Zhang, C., Xue, G., et al. (2023). Prediction of seismic acceleration response of precast segmental self-centering concrete filled steel tube single-span bridges based on machine learning method. Engineering Structures, 279: 115574. https://doi.org/10.1016/j.engstruct.2022.115574

[6] Du, H., Wang, H., Jia, Y. (2024). Research on intrusion detection of stacking LSTM hyperparameters optimized by adaptive genetic algorithm. Journal of Inner Mongolia University of Technology, 43(3): 271-277. https://doi.org/10.13785/j.cnki.nmggydxxbzrkxb.2024.03.013

[7] Feng, Z., Yan, C. (2023). Analysis of sensitive factors of pier Top deformation of highway subgrade crossing high-speed railway bridge. Journal of Inner Mongolia University of Technology, 42(2): 178-183.

[8] Liu, J., Bao, D., Liu, X., Liu, D., Wu, S., Wang, P. (2023). Safety analysis of umbrella wind turbine structure with different shrinkage angles. Journal of Inner Mongolia University of Technology, 42(2): 149-156.

[9] Catbas, F.N., Susoy, M., Kapucu, N. (2006). Structural health monitoring of bridges for improving transportation security. Journal of Homeland Security and Emergency Management, 3(4): 13. https://doi.org/10.2202/1547-7355.1217

[10] Bogaert, P., Van Oyen, H., BRIDGE Health. (2017). An integrated and sustainable EU health information system: National public health institutes' needs and possible benefits. Archives of Public Health, 75: 3. https://doi.org/10.1186/s13690-016-0171-7

[11] Yang, J., Bao, Y., Sun, Z., Meng, X. (2024). Computer vision-based real-time identification of vehicle loads for structural health monitoring of bridges. Sustainability, 16(3): 1081. https://doi.org/10.3390/su16031081

[12] Zou, L., Feng, W., Masci, O., Nico, G., Alani, A.M., Sato, M. (2024). Bridge monitoring strategies for sustainable development with microwave radar interferometry. Sustainability, 16(7): 2607. https://doi.org/10.3390/su16072607

[13] He, X., Tan, G., Chu, W., Zhang, S., Wei, X. (2022). Reliability assessment method for simply supported bridge based on structural health monitoring of frequency with temperature and humidity effect eliminated. Sustainability, 14(15): 9600. https://doi.org/10.3390/su14159600

[14] Lei, X., Sun, L., Xia, Y., He, T. (2020). Vibration-based seismic damage states evaluation for regional concrete beam bridges using random forest method. Sustainability, 12(12): 5106. https://doi.org/10.3390/su12125106

[15] Zhang, S.Y., Wang, Y.L., Yu, K.P. (2022). Steady-state data baseline model for nonstationary monitoring data of urban girder bridges. Sustainability, 14(19): 12134. https://doi.org/10.3390/su141912134

[16] Sun, S., Jiao, S., Hu, Q., Wang, Z., Xia, Z., Ding, Y., Yi, L. (2023). Missing structural health monitoring data recovery based on bayesian matrix factorization. Sustainability, 15(4): 2951. https://doi.org/10.3390/su15042951

[17] Zhong, G., Bi, Y., Song, J., Wang, K., et al. (2023). Digital integration of temperature field of cable-stayed bridge based on finite element model updating and health monitoring. Sustainability, 15(11): 9028. https://doi.org/10.3390/su15119028.

[18] Verzobio, A., Bolognani, D., Quigley, J., Zonta, D. (2022). Quantifying the benefit of structural health monitoring: Can the value of information be negative? Structure and Infrastructure Engineering, 18(4): 573-594. https://doi.org/10.1080/15732479.2021.1890139

[19] He, H., Wang, W., Zhang, X. (2019). Frequency modification of continuous beam bridge based on co-integration analysis considering the effect of temperature and humidity. Structural Health Monitoring, 18(2): 376-389. https://doi.org/10.1177/1475921718755573

[20] Gilligan, T., Alamgir, H. (2008). Bridging the knowledge gap: an innovative surveillance system to monitor the health of British Columbia's healthcare workforce. Canadian Journal of Public Health, 99: 478-482. https://doi.org/10.1007/BF03403780

[21] David, M., Schwedler, G., Reiber, L., Tolonen, H., et al. (2020). Learning from previous work and finding synergies in the domains of public and environmental health: EU-funded projects BRIDGE Health and HBM4EU. Archives of Public Health, 78: 78. https://doi.org/10.1186/s13690-020-00460-9

[22] Tonnesen, M., Hedeager Momsen, A.M. (2023). Bridging gaps in health? A qualitative study about bridge-building and social inequity in Danish healthcare. International Journal of Qualitative Studies on Health and Well-being, 18(1): 2241235. https://doi.org/10.1080/17482631.2023.2241235